Laser Damage Inspection Final Report Laboratory Directed Research and Development Program 00-ERD-067

J.T. Salmon, J.M. Brase, E.S. Bliss, C.J. Carrano, L. M. Kegelmeyer, M.G. Miller, C.D. Orth, and R.A. Sacks

February 26, 2001

U.S. Department of Energy

Lawrence
Livermore
National
Laboratory

DISCLAIMER

Laser Damage Inspection
Final Report
Laboratory Directed Research and Development Program
00-ERD-067

J.T. Salmon, J.M. Brase, E.S. Bliss, C.J. Carrano, L. M. Kegelmeyer,
M.G. Miller, C.D. Orth, and R.A. Sacks

Introduction

Large, high-power laser systems are often designed as reimaging multipass cavities to maximize the extraction of energy from the amplifiers. These multipass cavities often have vacuum spatial filters that suppress the growth of beam instability via B-integral effects. These spatial filters also relay images of laser damage, often nearly superimposing these images in common planes. Also, the fluence damage threshold limits the minimum size of the optics. When used as vacuum barriers in the spatial filters, these large optics present a safety hazard from the risk of implosion if the laser damage were sufficiently large.

The objective of the project was to develop algorithms and methods for optical detection and characterization of laser-induced damage of optics. The system should detect small defects (about 5% of the critical size), track their growth over multiple laser shots, and characterize the defects accurately so that the optic can be replaced (at 25% of the critical size) and, hence, minimize the risk of implosion. The depth of field must be short enough to isolate the damaged vacuum barrier from other damaged optics in the beamline, and the system should also be capable of inspecting other optics in the beamline, since damage on one optic can subsequently damage subsequent optics.

Laser induced damage starts as a small (<<1mm) crater and grows as material is removed on subsequent laser shots. The highly fractured rough surface of the crater scatters light from the illuminating inspection beam. This scattered light is imaged by the inspection system. Other types of defects may occur as well including inclusions in the bulk glass, tooling marks, and surface contamination. This report will discuss the detection and characterization of crater-like surface defects although the general techniques may prove useful for other types of defects.

The work described here covers the development of an image processing approach and specific algorithms for defect detection and characterization in dark and bright field images. Supporting tasks include the collection of experimental images from a physical model of a representative beamline of a high-power laser and development of a propagation model of the same beamline. This beamline includes multipass amplifiers and spatial filters. While the experimental model and the numerical model used to verify the algorithms presented here are of a specific architecture, the general image processing approach taken here should be applicable to any high-power laser system.

Our approach to image processing development has three main components. First, determine the smallest detectable defect. Second, determine the accuracy of the measurement of a defect that is 25% of the critical size. Third, develop and demonstrate a process for inspecting the set of spatial filter optics that would normally be vacuum-loaded in an actual high-power laser system. The method must account for multiple passes and nearly overlapping multiple conjugate planes in the beamline.

The experimental system

The development of image processing techniques and algorithms for defect detection and characterization requires images that correspond in known ways to images in an actual laser system. The method, specific algorithms, and performance estimates presented here depend on this assumption. The images used here were obtained with a scaled version of a NIF beamline and with an imaging system similar in design to the Large Optics Damage Inspection System (LODI). This method consists of propagating a beam through the optics collinear to the laser beam and sampling the beam after it exits the last spatial filter. Although this method contains information of defects on every optic, this information must be inverted to yield information about any given optic.

The goal of the system is to produce images of laser-induced defects with signal and noise characteristics that closely match those produced by LODI. For this purpose a scaled laboratory model was assembled shown in Fig. 1. The model scaled to $1/10$ length and to $1/\sqrt{10}$ (0.316) in width. This scaling ratio of length to width makes the image of scaled defects independent of the actual scale factors used.
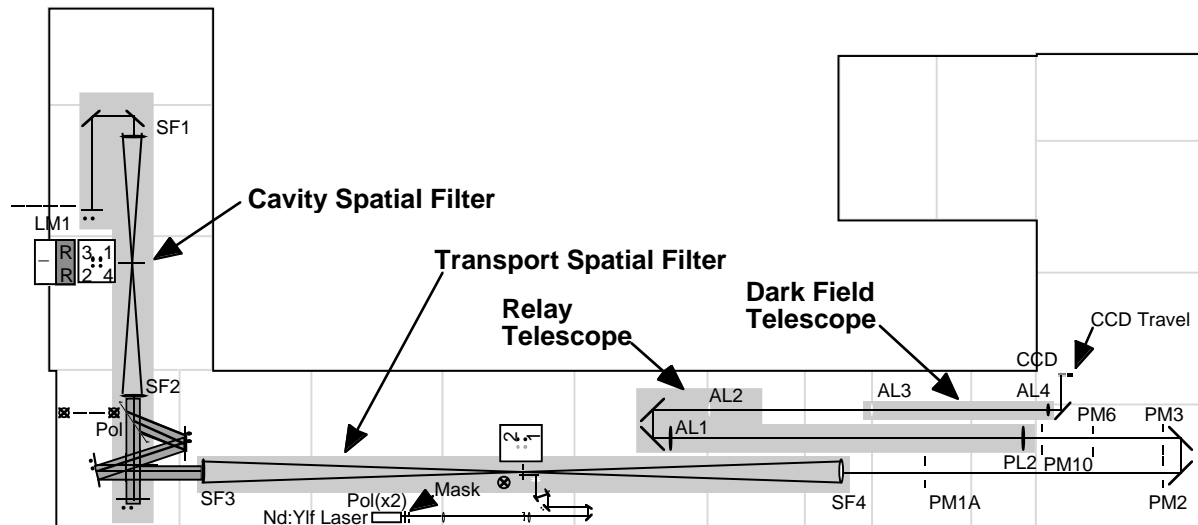

Figure 1. Layout of the experimental model of the high-power, multipass laser system and optical damage inspection system.

The model has two spatial filters, the Cavity Spatial Filter (CSF) and the Transport Spatial Filter (TSF). The CSF is in a 4-pass cavity with the main amplifier normally located between the CSF and the end mirror LM1. The spatial filter lenses nearly image LM1 to LM2. The TSF contains the beam insertion mirror near the pinhole plane, and the final power amplifier would normally be in collimated space next to SF3. The probe beam is injected in the TSF toward the left and enters the CSF via a polarizer at Brewster's angle. The beam enters the CSF at an angle, which changes from pass to pass, which causes the beam to cross the pinhole plane at a different displacement from the optic axis of the CSF. A half-wave plate rotates the polarization of the beam by 90° on pass 1 and pass 4, which keeps the beam in the CSF cavity until pass 4. The beam then passes through the TSF and crosses the pinhole plane of the TSF displaced from the injection point. The exit mirror of the TSF (SF4) collimates the beam. The probe beam is relayed and resized by a relay telescope and then relayed by a final telescope (Dark Field Telescope) that has an insertable dark stop inserted on-axis at the focus of the telescope.
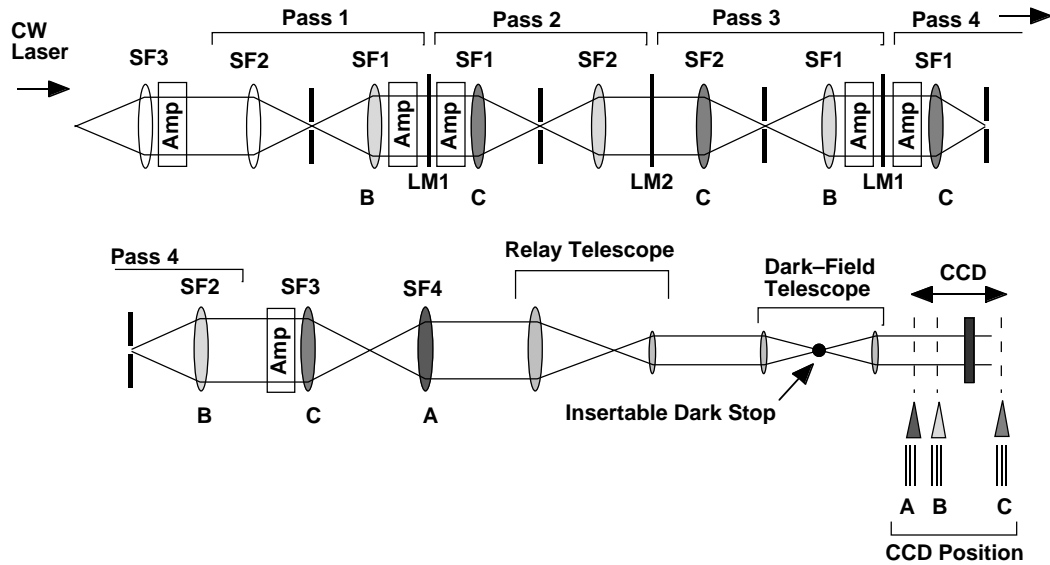

Figure 2. Unfolded optical schematic of the beamline in this study. Planes that are in focus for CCD positions A, B, or C are marked with the same letter in the optics chain. Amplifiers, located (1) between SF1 and the end mirror LM1 and (2) in collimated space next to SF3, were not modeled.

The image planes corresponding to various focus positions of the CCD detector in this experimental model are shown in Fig. 2. When the detector is in position A all planes marked with the letter A are in focus (SF4 only for position A) and so on. Note that, in general, multiple optics are in focus for a given camera position, which is one of the issues that the image processing approach must resolve.

The system acquires images from a 1K x 1K portion of a 2K x 2K scientific-grade CCD camera with 12-bit resolution. In addition, the system collects image acquisition parameters such as pinhole status in the spatial filters, camera focus

position, and exposure time. The image processing system generates defect lists that go into a database and can display an optional defect map with annotated optic location and defect size. An alarm signal can notify the user when a defect above a preset threshold size is detected. The interfaces to the image acquisition system have been specified in detail but the output interfaces have not.

Numerical Modeling Code

We used PROP92[1] to simulate numerically optical propagation through the experimental model. This code helped to determine the original design of NIF after years of consistent agreement with experimental results in other high-power laser systems. PROP92 uses a Fourier technique to solve the nonlinear Schrödinger equation, yielding a representation of the single-polarization complex electric field $E(x,y,z,t)$ in two transverse directions (x,y) plus time (i.e., in 2D) as the beam transports through a chain of optical elements. Propagation is computed in the far field with slowly varying $(\partial u/\partial t << \omega_0 u)$ and paraxial $(\partial^2 u/\partial z^2 << k_0 \partial u/\partial z)$ approximations using a Fourier transform and its inverse according to

$$u(\mathbf{r}, z + \delta z) = \frac{R_0}{R} \int \frac{d^2\kappa}{(2\pi)^2} e^{i\frac{R_0}{R}\mathbf{k}\cdot\mathbf{r}_e - \frac{iR_0}{2k_0R}\kappa^2\delta z} \times \int d^2\mathbf{r}' e^{-i\mathbf{k}\cdot\mathbf{r}'} u(\mathbf{r}', z, t)$$

Here the wave number $k_0 = n_0\omega_0/c$ where n_0 is the index of refraction in the medium of propagation, ω_0 is the laser's optical frequency, and c is the speed of light in vacuum. The residual wave function $u(\mathbf{r},z,t)$ is left after the removal of (1) the dominant plane-wave portion of the beam and its center-point position, (2) tilt κ, and (3) curvature $R = R(z+\delta z)$ and $R_0 = R(z)$ have been removed from $E(x,y,z,t)$. Since u is represented on a discrete mesh, the continuous transform above is calculated by a discrete fast Fourier transform (FFT). PROP92 differs from a scalar diffraction code in its ability to include linear and nonlinear-damage packages, which were not needed here owing to the low power of the probe beam.

The numerical model includes a phase map of the optical path difference for every optic in the laser. The phase maps of the lenses were measured on a phase-measuring interferometer double-pass with a reference sphere to autocollimate the return beam to the interferometer. Tilt and piston were removed from the phase maps. Other optics (mirrors) had generic statistical aberration files obtained from measured NIF large optics. To maintain the correct orientation of the phase maps, we oriented the maps forward or rearward according to the placement of the optics in the beam line. The model also placed rectangular masks to match the aperture of each optic. In addition, for the final telescope optics, we removed the net power terms for each telescope over the width of the beam to make the telescopes afocal. This adjustment makes the telescopes telecentric imaging systems but yields higher phase errors at the edge of the aperture.

PROP92 was run with a 1024x1024 grid over a lateral area 10% larger than the injected beam size to closely match the CCD camera resolution in pixels of roughly 1kx1k over the beam size. From the distribution at the CCD the fluence is displayed using IDL code, and "pixelating" the results using a 9-point Lagrangian

interpolation (i.e., replacing each fluence value by a new value obtained from a 9-point Lagrangian interpolation using the values at that point and its surrounding 8 neighboring points). We processed the resultant images using the IDL code via a 400 by 400 interpolation grid.

We simulated a dark stop for dark-field images by inserting a one-micron-focal-length FILTER command behind the first lens of the dark-field telescope. The filter has an angular blockage corresponding to a 1.63-mm diameter mask at the focus of the telescope. We simulated one row of defects at SF3 by inserting 12 MASK commands representing opaque spots having diameters 1.0, 0.9, 0.8, 0.7, 0.6, 0.5, 0.4, 0.3, 0.2, 0.15, 0.125, and 0.10 mm, which occupied 7.4 to 0.74 grid-point separations, respectively. We ignored thermal effects and image astigmatism caused by tilted amplifier slabs. We also used the same beam propagation angles used in the experimental model, including the axial alignment of the beam after SF4 obtained by the tilt of SF4.

Comparison of numerical and experimental models

Figure 3 shows the profiles of the numerical and experimental images of a 0.9-mm-diameter dot at SF3. The sharpness of the simulated image matches rather closely the sharpness observed experimentally in bright field, and the widths differ by about 2% (FWHM). The contrast in dark-field images is also similar, although the numerical simulations have more background noise. Thus, the simulations reproduce what is seen experimentally, so numerical modeling can now be used as a tool to answer various design questions.
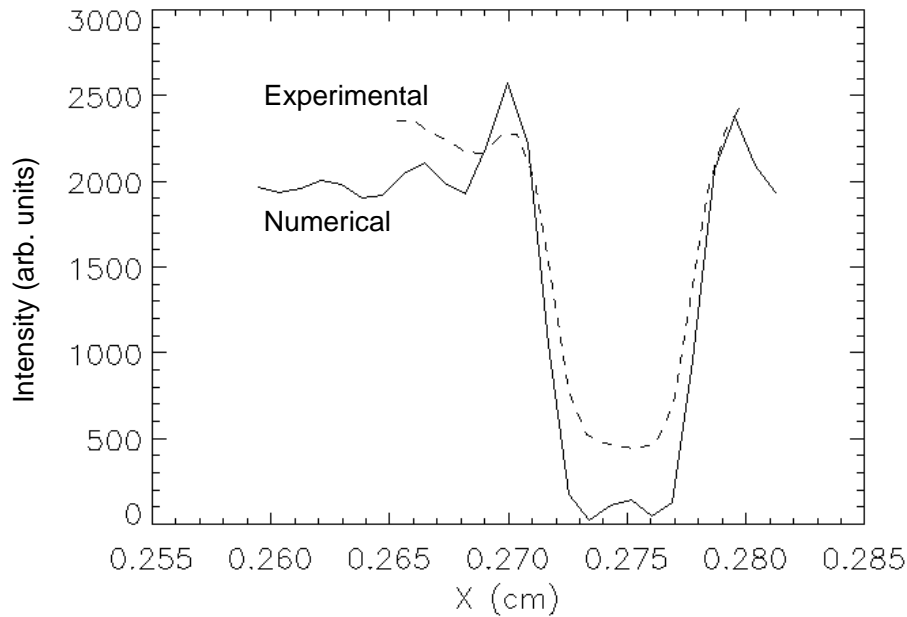

Figure 3. Lineouts of experimental and numerical images of a 0.9-mm-diameter opaque dot at SF3 as seen in bright field.

Single defect detection performance

Two sets of experiments have established the detectability of defects in the laboratory system. The first experiments placed an array of chrome on glass dots with diameters ranging from less than 0.1 mm to 1.2 mm at each optic position (SF1, SF2, SF3, and SF4) and recorded images. In the second experiment a mask with a set of four machined defects that more closely approximate laser-induced damage replaced the chrome dot mask. The results of analysis of these images are given in this and the following sections.

Figures 4 and 5 shows one example of the bright field and dark field images used to measure detectability for varying defect sizes. The known defects are the four dark spots near the bottom of Fig. 4 and the corresponding bright spots in Fig. 5. From left to right the defect sizes are 1.55 mm, 0.75 mm, 0.57 mm, and 0.36 mm. Lineouts through the center of the 1.55 mm defect are shown in Fig. 6 for bright field and Fig. 7 for dark field. These measurements are used to calculate the peak signal levels for each defect size.

To calculate the signal-to-noise ratio (SNR) for a defect image we measure the image modulation due to the defect and the noise or clutter level in the image. The signal is defined as the peak value of the modulation in the defect image

$$\text{Signal} = I_{max} - I_{back}$$

where I_{max} is the peak pixel value in the defect and I_{back} is the mean pixel value in the background. The image clutter is defined as the apparently random fluctuations in the background. The main source of these fluctuations appears to be out of focus scattering objects on other optics in the system. Some may be defects on out-of-focus optics; some may be distributed surface roughness. To measure the clutter level we select a region with no identified defects and compute the standard deviation of the pixel values in the region. Then the SNR is defined as

$$\text{SNR} = (I_{max} - I_{back}) \,/\, \sigma_{background}$$

where $\sigma_{background}$ is the rms clutter in the background intensity. Figures 8 and 9 show the measured SNR's for defects as a function of the actual size of the defect for bright and dark field images. The SNR values are plotted for both the four-defect mask and for the chrome dot mask.

Generally a SNR of > 5 is required for reliable detection of a peak in random noise. For the defects tested with these particular clutter backgrounds the tests suggest that a bright field defect must be greater than 0.2 mm to be reliably detected while for dark field we can reliably detect less than 0.1 mm. These minimum detectable signal levels, however, depend highly on the clutter backgrounds and exposure times.

The size of a defect that is resolved in the image may be measured in two ways: integrated intensity and direct measurement of the size or area. Direct measurement of the size is useful for defects much larger than the resolution of the imaging

system. This method relies on fewer assumptions and does not require calibrations or lookup tables for each optic; however, it becomes unreliable as the defect size approaches the resolution of the imaging system.
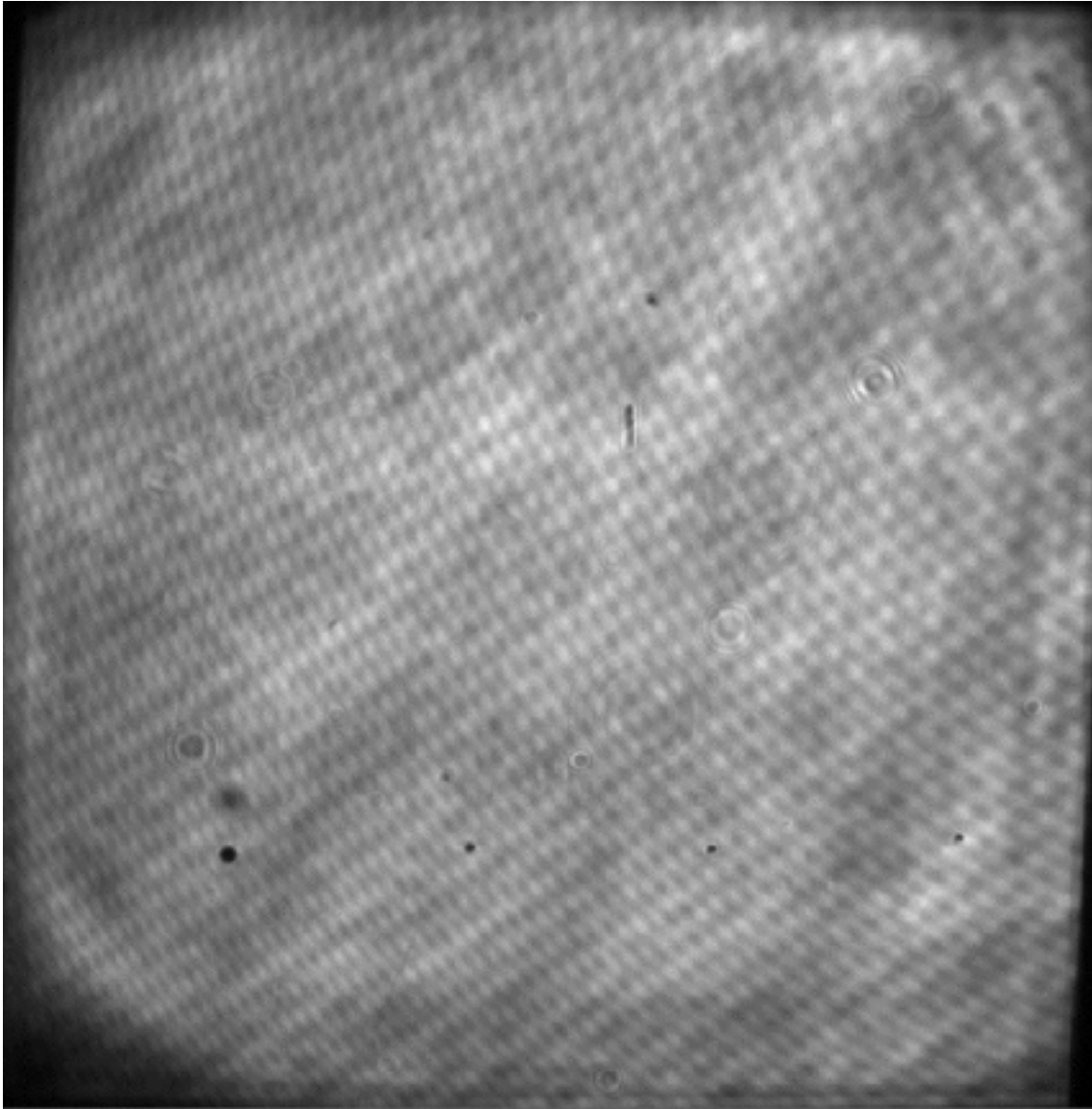

Figure 4. Example bright field image from the LODI laboratory system. The image is focused at SF3. The four-defect mask is installed at SF3.

The integrated intensity for a defect image is proportional to the total energy scattered by the defect and should be directly related to the defect size. This relationship is plotted in Fig.s 10 and 11 for the two sets described in the earlier section. In particular, Fig. 10 shows a consistent linear relationship between integrated intensity and defect size.

Figure 5. Example dark field image from the LODI laboratory system. The image is focused at SF3. The four-defect mask is installed at SF3.

Beamline inspection approach

From the previous section the SNR for dark-field images is nearly 90 times that for bright-field images. Hence, dark field images are preferred for detection of defects and for estimates of position; however, dark-field images do not readily provide a valid estimate of defect size for large, resolved defects. The dark stop acts as a high-pass filter, and the image consists mainly of the enhanced edges of the defect. A possible approach (not yet developed) is to make size estimates for large defects from bright field images that do not have this problem. This will be discussed later.
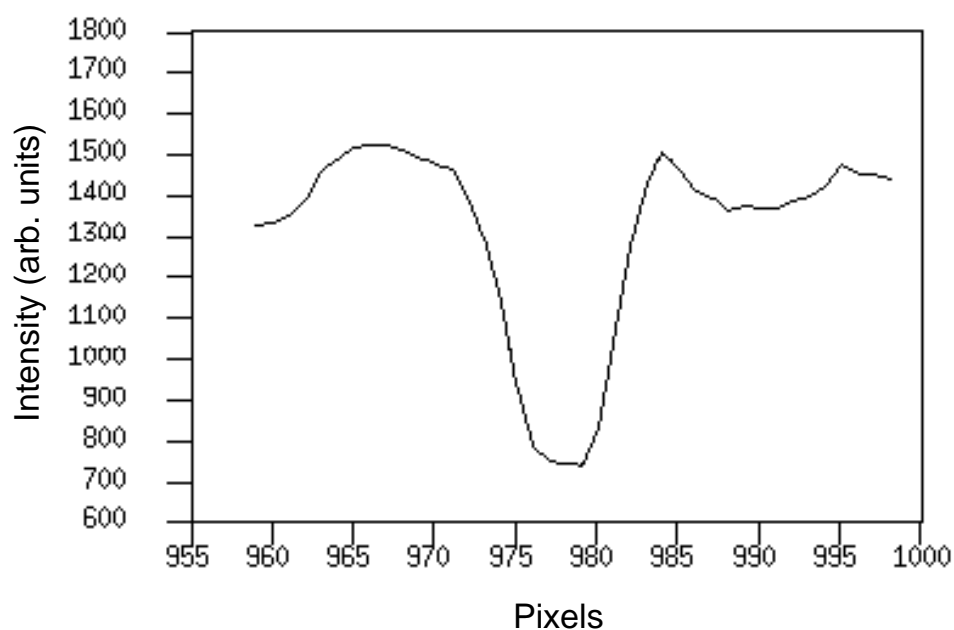
Figure 6. Lineout through the center of the 1.55 mm defect from the bright field image. X-axis units are pixels (0.13 mm/pixel) and the y-axis units are digital numbers.
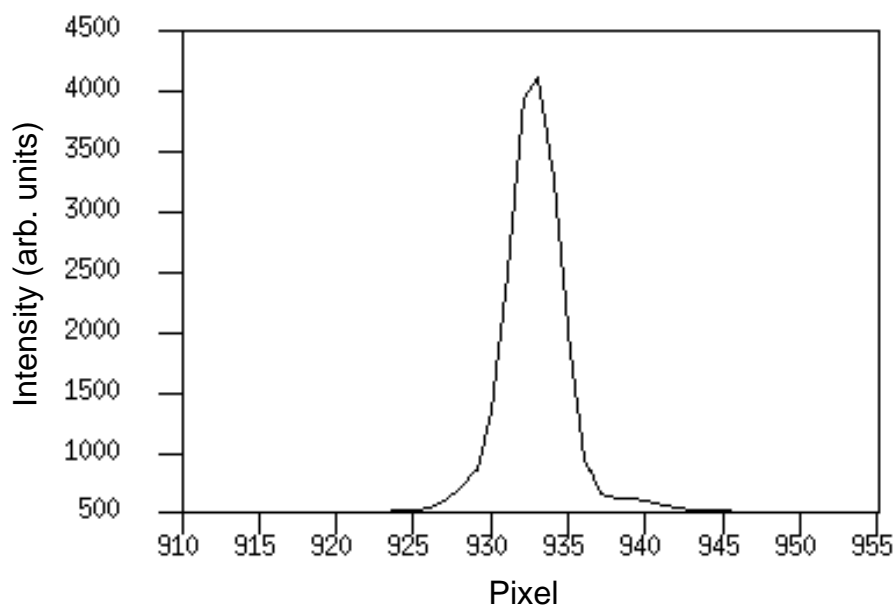

Figure 7. Lineout through the center of the 1.55 mm defect from the dark field image. X-axis units are pixels (0.13 mm/pixel) and the y-axis units are digital numbers.
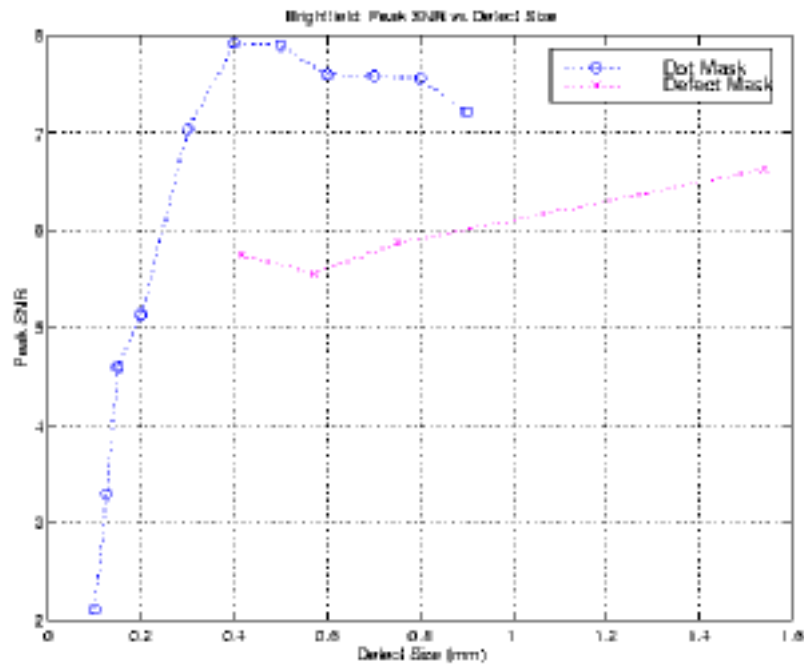
Figure 8. Bright field signal to noise ratio measured for two sets of defects. The first is the chrome dot mask and the second is the four-defect mask.
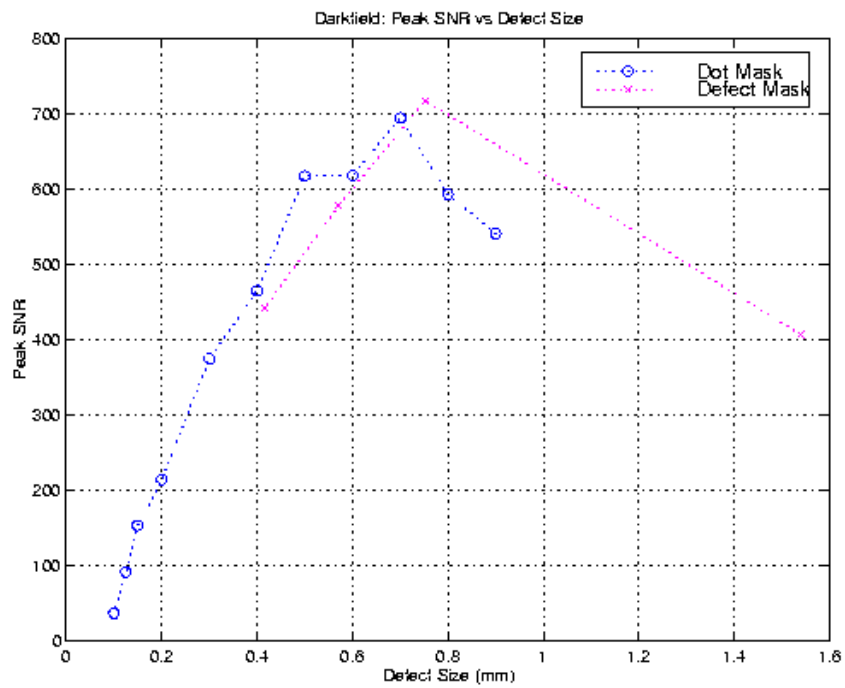

Figure 9. Dark field signal to noise ratio measured for two sets of defects. The first is the chrome dot mask and the second is the four-defect mask.
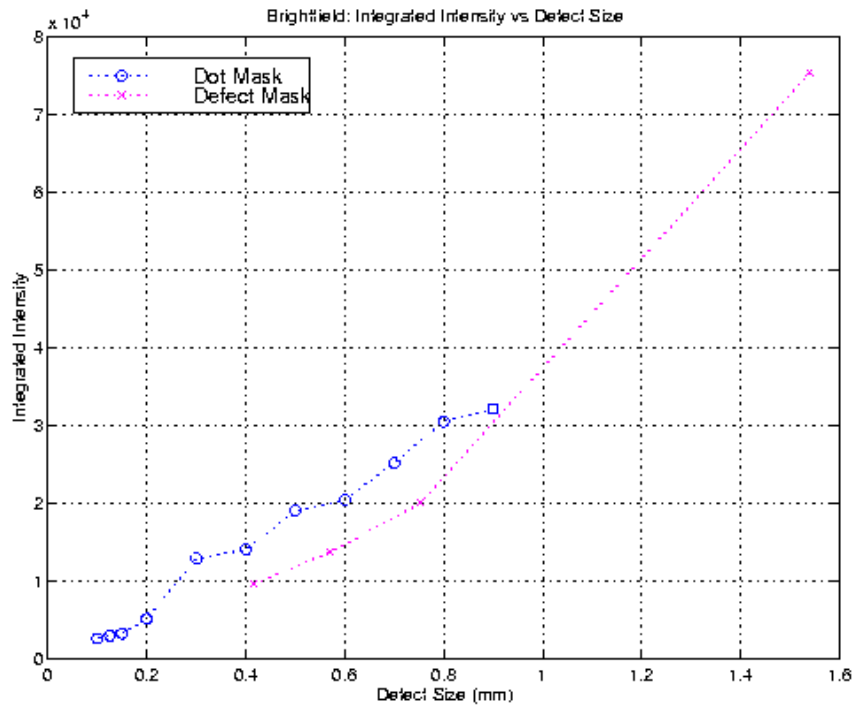
Figure 10. Integrated intensity for chrome dot mask and four-defect mask in bright field images.
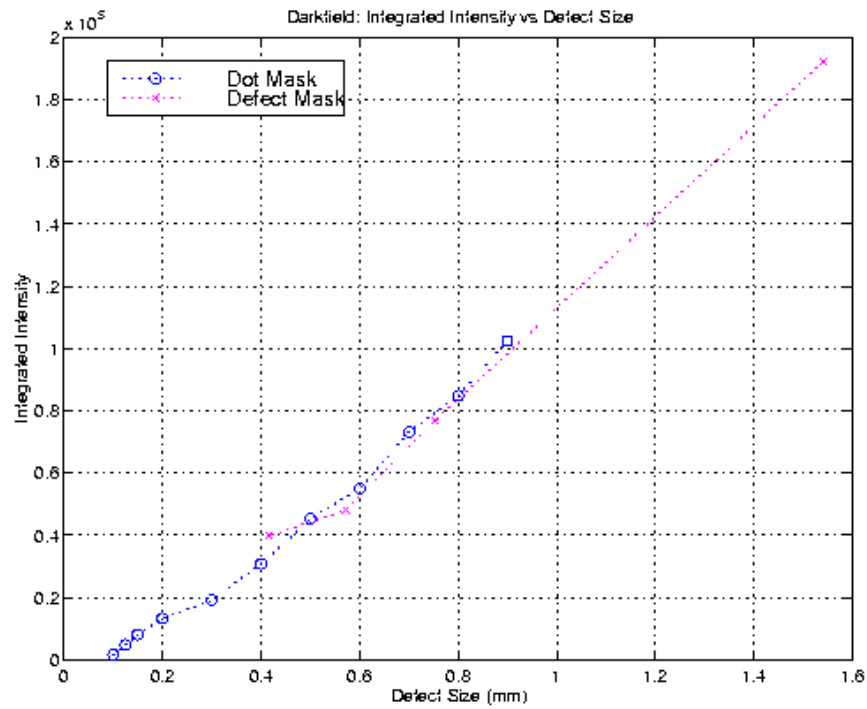

Figure 11. Integrated intensity for chrome dot mask and four defect mask in dark field images.

The above results assume images of single defects on a single, known optic. The inspection of a real beamline is complicated by multiple passes through many of the optics yielding (1) multiple images of the defects from a single optic (some in focus and others out of focus) with small translations from pass to pass and (2) multiple object planes in focus on the detector at any given position of the detector.

To resolve these difficulties we acquire a sequence of images for a given beamline with a combination of spatial filter pinholes and focus positions to resolve the ambiguities. Inserting a low-pass spatial filter (a small pinhole) minimizes image information from object planes prior to the spatial filter. This technique is allowed by the lateral translation of the beam focus from pass to pass and eliminates many of the multiple images of defects that confuse the interpretation of the image. The image sequence for each beamline is defined in Table I. For each image both a dark-field image and a bright-field image are acquired.

Table I. Spatial filter and camera focus positions in the image sequence for inspecting a full multipass laser beamline. Filter Position indicates those spatial filter pinholes that are in the beamline (all other pinholes are out of the beamline). See Fig. 2 for definitions of positions A–D.

Image	Filter Position	CCD Position	Optics in Focus
1	CSF Passes 1 & 2	B	SF1, SF2
2	CSF Passes 1 & 2	C	SF1, SF3
3	CSF Passes 1–3	B	SF2
4	CSF Passes 1–3	C	SF3
5	CSF Passes 1–4 TSF Passes 1 & 2	A	SF4

Two main issues must be resolved by the image processing. First, double images of defects on SF1 are still in images 1 and 2. Second, both SF1 and SF2 defects are on image 1, and SF1 and SF3 defects are on image 2. The information from images 1, 2, and 3 must be combined in the image processing algorithms to give a consistent set of defects for SF1.

Image processing algorithms and results

Based on the image sequence defined in Table I, the following image processing methodology addresses the issues discussed above. The image processing sequence of operations are defined in the block diagram in Fig. 12.

The image sequence collected in the first operation is the sequence of dark and bright field images defined in Table I. Dark field images are used throughout the detection process until the integrated intensity measurement in the last set of operations where bright field images may be used for large defects.
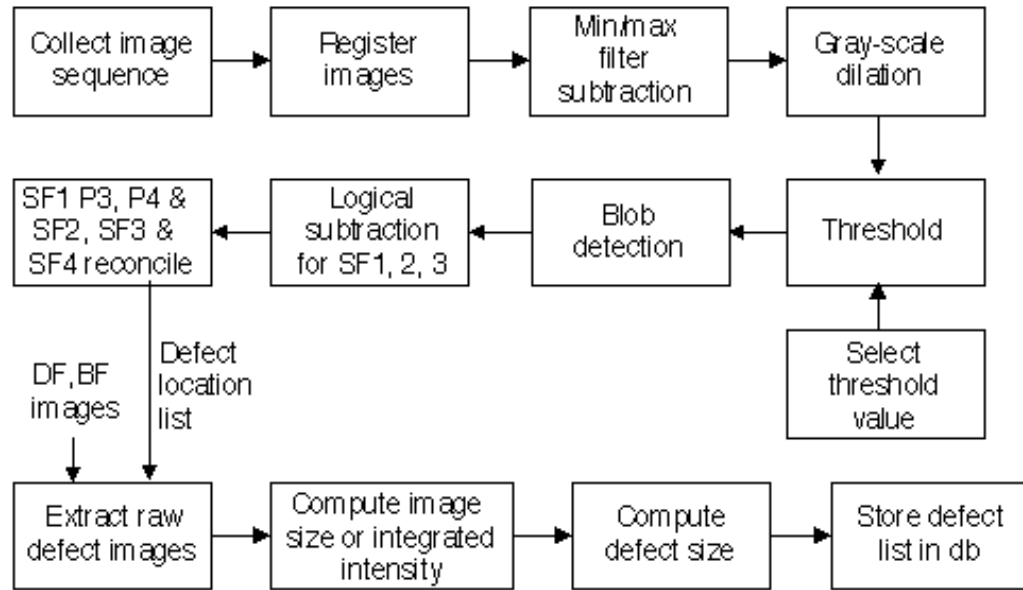
Figure 12. Block diagram of the image processing methodology used to analyze images from a single NIF beamline.

The dark field images are first registered to a fixed coordinate system. In the first test of the approach, images 1 and 3 are manually registered to each other, and images 2 and 4 are also manually registered to each other, because detection lists from each pair of images must be combined in the logical subtraction operation. In the long term we must register the full set of images to an absolute coordinate system based on image features to be able to track defect growth over time. Techniques for this registration will be developed in the future.

Min–max filter subtraction is a technique that flattens low spatial frequency variations in the image background and reduces image clutter[2]. The spatial frequency response of the operation is designed to ignore defects in the size range of interest. Gray-scale dilation expands the potential objects to create regions-of-interest for further measurement and analysis.

A threshold applied to the image reveals pixels that might be part of defect images. Global statistics of the enhanced dark field image determines the threshold value, which is currently applied by the user. This process will be automated, perhaps based on local statistics, in future work. Blob detection operates on the binary image and combines groups of connected pixels that are then listed as a detected defect. Adjustable parameters control how large a gap is allowed in a blob and the minimum blob size.

The raw detected defect location lists from the blob detector are then compared to reconcile duplicate defects in images 1 and 3 and images 2 and 4 – a logical subtraction operation performed on the defect lists. The resulting two defect lists for SF1—one from image 1 and one from image 2—must be reconciled given that they

have a known shift between them (pass 3 to pass 4 in the CSF). This operation gives us the final defect location list for the set of optics.

Using the final defect location lists, we extract local regions around the defects in the original raw images raw images—dark field for small defects (<2 mm?) and bright field for large defects. The integrated intensity for the given defect yields the defect size from a calibration curve similar to that in Fig. 11. The detection list may be displayed in the form of a detection map as shown in Fig. 13. The map shows the defect location in a fixed coordinate system and gives the optic containing the defect and its estimated transverse size.
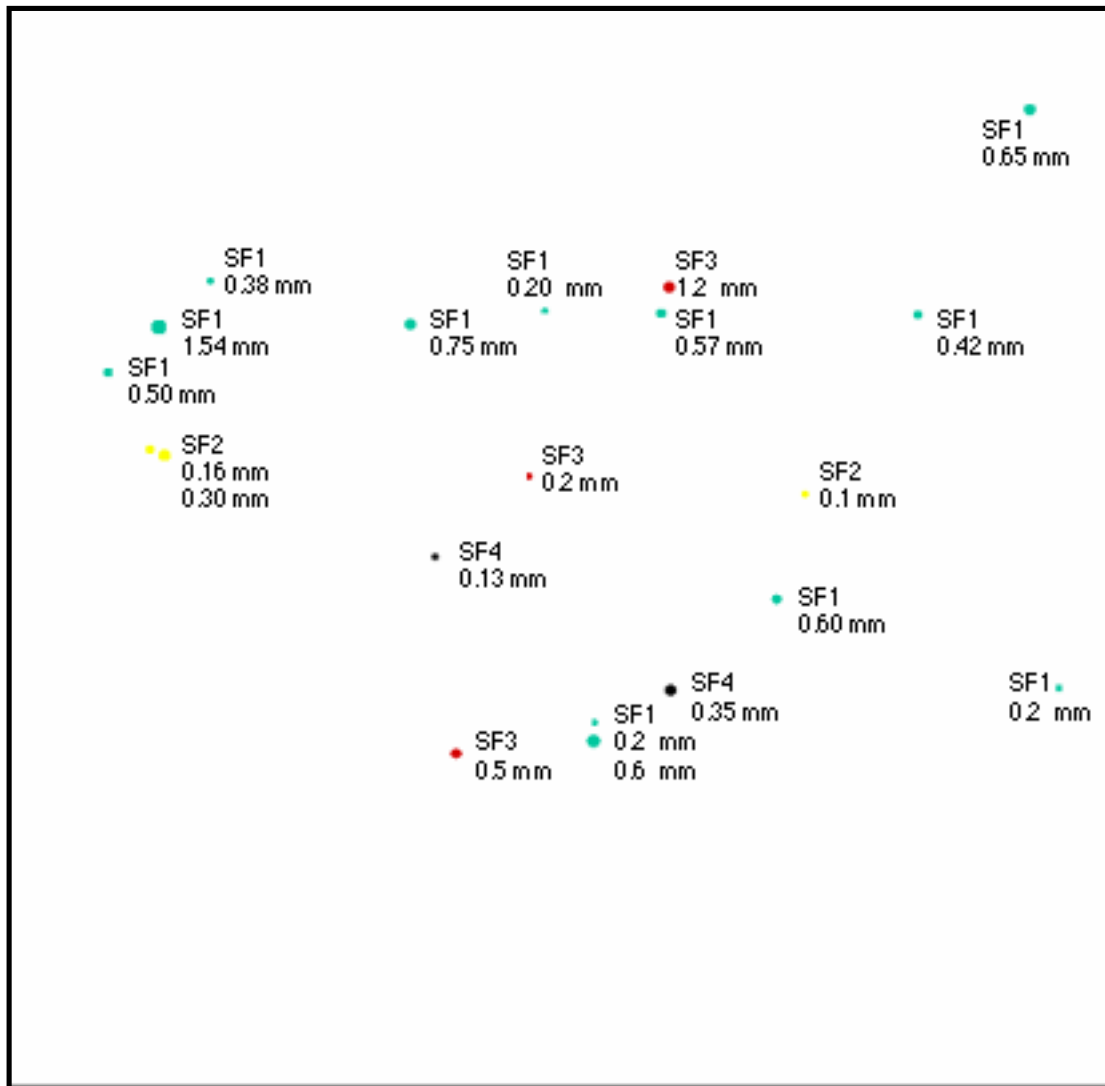

Figure 13. Composite detection map showing defects detected on all optics by the image processing procedure of Figure 12. Each defect is labeled with the optic it is on and its diameter estimate in mm. For this test the four-defect mask was placed at SF1. The color of the defect marker also indicates which optic it is on.

Conclusion

We have demonstrated a baseline image processing methodology for detecting and characterizing multiple defects on multiple optics in a model of a high-energy, multipass laser system with vacuum spatial filters. An overall framework has been implemented in an interactive image processing system that measures the defect size and identifies the damaged part even when multiple parts are conjugate to each other. This system will serve as a foundation for further development and performance optimization. Although this methodology focused on a particular laser design, it can be applied to any similar design.

Dark field imaging has a high enough SNR for reliable detection and defect size estimation as long as the density of defects results in a low probability of in-focus defects overlapping in the detector plane. The variability of SNR and size measurements is not yet understood and need further study.

References

[1] R. A. Sacks, M. A. Henesian, S. W. Haney, J. B. Trenholme, "The PROP92 Fourier Beam Propagation Code," *ICF Annual Report 1996*, University of California, Lawrence Livermore National Laboratory, Report UCRL-LR-105821-96 (1997) 207–213.

[2] PW Verbeek, HA Vrooman, LJ Van Vliet, "Low Level image processing by max-min filters. Signal Process 17:249-258, 1988.